Occludin stalls HCV particle dynamics apart from hepatocyte tight junctions, promoting virion internalization

Maika S Deffieu, Camille M H Clément, Cristina M Dorobantu, Emma Partiot, Yonis Bare, Orestis Faklaris, Benjamin Rivière, Nilda Vanesa Ayala-Nunez, Thomas F Baumert, Philippe Rondé, et al.

▶ To cite this version:

Maika S Deffieu, Camille M H Clément, Cristina M Dorobantu, Emma Partiot, Yonis Bare, et al.. Occludin stalls HCV particle dynamics apart from hepatocyte tight junctions, promoting virion internalization. Hepatology, 2022, 76 (4), pp.1164-1179. ⟨10.1002/hep.32514⟩. ⟨hal-03739439⟩

HAL Id: hal-03739439
https://hal.science/hal-03739439v1

Submitted on 27 Jul 2022

Occludin stalls HCV particle dynamics apart from hepatocyte tight junctions, promoting virion internalization

Maika S. Deffieu[1,2,#], Camille M.H Clément[1,2,3,4,#], Cristina M. Dorobantu[3,4], Emma Partiot[1,2], Yonis Bare[1,2], Orestis Faklaris[5], Benjamin Rivière[6], Nilda Vanesa Ayala-Nunez[1,2], Thomas F. Baumert[3,4,8], Philippe Rondé[3,7], Yves Mély[3,7], Vincent Lucansky[3,4], Raphael Gaudin[1,2,*].

[1] Institut de Recherche en infectiologie de Montpellier (IRIM) CNRS, 34293 Montpellier, France
[2] Université de Montpellier, 34090 Montpellier, France
[3] Université de Strasbourg, 67000 Strasbourg, France
[4] INSERM, Institut de Recherche sur les Maladies Virales et Hépatiques, 67000 Strasbourg, France
[5] BCM, University of Montpellier, CNRS, INSERM, Montpellier, France
[6] CHU Montpellier, Laboratoire d'Anatomie et Cytologie Pathologiques – CRB, 34295 Montpellier, France
[7] UMR 7021 CNRS, Laboratoire de Bioimagerie et Pathologies, Université de Strasbourg, Faculté de pharmacie, 67401 Illkirch, France
[8] Pole Hépato-digestif, Hôpitaux Universitaires de Strasbourg, Institut Hospitalo-universitaire, 67000 Strasbourg, France

[#] These authors contributed equally
Present addresses:
CD: Janssen Vaccines and Prevention B.V. Newtonweg 1, 2333 CP Leiden PO Box 2048, 2301 CA Leiden, The Netherlands.
NVAN: Empa - Swiss Federal Laboratories for Materials Science and Technology. Lerchenfeldstrasse 5, 9014 St. Gallen, Switzerland.
VL: Comenius University in Bratislava, the Jessenius Faculty of Medicine in Martin (JFMED CU), Biomedical Center Martin, Mala Hora 4C, 036 01 Martin, Slovakia.

* Corresponding author: Raphael Gaudin. **Email:** raphael.gaudin@irim.cnrs.fr

Keywords: virus-host interactions; human liver; live cell imaging; CRISPR; flavivirus

Abstract

Numerous hepatitis C virus (HCV) entry factors have been identified and yet, information regarding their spatiotemporal dynamics is still limited. Specifically, one of the main entry factors of HCV is occludin (OCLN), a protein clustered at tight junctions (TJs), away from HCV landing site. Thus, whether HCV particles slide toward TJs or conversely, OCLN is recruited away from TJs remains debated. Here, we generated CRISPR/Cas9 edited Huh7.5.1 cells expressing endogenous levels of EGFP-OCLN and showed that incoming HCV particles recruit OCLN outside TJs, independently of claudin-1 expression, another important HCV entry factor located at TJs. Using *ex vivo* organotypic culture of hepatic slices obtained from human liver explants, a physiologically relevant model that preserves the overall tissue architecture, we confirmed that HCV associates with OCLN away from TJs. Furthermore, we showed by live cell imaging that the increased OCLN recruitment beneath HCV particles correlated with lower HCV motility. To decipher the mechanism underlying virus slow-down upon OCLN recruitment, we performed CRISPR knock out of Claudin1 (CLDN1), a HCV entry factor proposed to act upstream of OCLN. Although CLDN1 KO potently inhibits HCV infection, OCLN kept accumulating underneath the particle, indicating that OCLN recruitment is CLDN1-independent. Moreover, inhibition of the phosphorylation of Ezrin, a protein involved in HCV entry that links receptors to the actin cytoskeleton, increased OCLN accumulation and correlated with more efficient HCV internalization. Together, our data provide robust evidence that HCV particles interact with OCLN away from TJs and shed novel mechanistic insights regarding the manipulation of transmembrane receptor localization by extracellular virus particles.

Main Text

Introduction

HCV chronically infects hepatocytes and induces liver diseases, including fibrosis, cirrhosis and ultimately may lead to hepatocarcinoma (HCC). HCC is a leading cause of cancer death (1) and despite the approval of an efficient treatment with a cure rate ≥ 90%, a vaccine is absent, cured patients are not protected against HCV re-infection, and long-term impact of the treatment is only partially understood. Indeed, pro-carcinogenic perturbations in the liver epigenome persist in cured patients (2). HCV is an enveloped positive-strand RNA virus from the *Flaviviridae* family. HCV particles enter cells through clathrin-mediated endocytosis (3, 4) and numerous entry factors have been reported to facilitate HCV attachment and internalization, including LDLR, CD81, SR-B1, Claudin1 (CLDN1), Occludin (OCLN), EGFR and Eph2A (5-7). Although the functional role of these entry factors has been investigated, little is known about the spatiotemporal dynamics of HCV-receptor interactions, and in particular, when, where, and how OCLN is recruited to facilitate virus entry.

OCLN is a tetraspan integral membrane protein and primarily localizes to TJs, although it has also been reported to localize at the leading edge of migrating cells (8, 9). OCLN has been described as involved in late entry events of HCV, likely being the latest one (10-12). Specifically, analyses of the temporal recruitment of the different HCV entry factors using blocking antibodies suggested that CD81, CLDN1, and OCLN are used in this order by the incoming particles (10). CD81 is thought to mediate virus attachment and to mobilize CLDN1 to initiate subsequent entry processes (13, 14). Because CLDN1 and OCLN are two tight junction (TJ) associated proteins, a "stick-and-seek" strategy (15) – in which viral particles are first landing on the cell surface, and subsequently sliding at the cell surface toward the TJs – was often used to represent how the viral particle would reach out to its receptors (16). An early spatiotemporal study performed in CD81-EGFP or GFP-Actin overexpressing Huh7.5 cells, failed at demonstrating the directed movement of HCV particles toward TJs (4), as opposed to the Coxsackie virus, for which clear redistribution of incoming virions toward TJs was demonstrated (17). Moreover, while the association between CD81 and CLDN1 is crucial to HCV infection, CD81 was not found at the TJ-associated pools of CLDN1 (13). These studies were performed in cell culture monolayers and in contrast, a study showed that HCV particles incubated with Huh7.5

cells grown in 3D, were distributed at the center of the spheroid, colocalizing with TJ markers (18). However, TJ localization of OCLN is not a prerequisite for HCV infection (19), and thus, whether HCV needs to reach TJs to infect hepatocytes remains unclear.

Here, we generated CRISPR/Cas9 gene edited Huh7.5.1 cells expressing endogenous levels of OCLN fused to EGFP to follow the dynamics of HCV-OCLN interactions in live, unperturbed cells. Quantitative 5D image analyses revealed that endogenous OCLN is recruited outside TJs to associate with incoming HCV particles. By high-resolution imaging of *ex vivo* infection of organotypic human liver slices, we confirmed in a physiologically relevant model that HCV particles associate with OCLN outside TJs. Mechanistically, we found that OCLN accumulation underneath HCV particles correlate with restricted virus movement. Finally, we showed that non-junctional OCLN recruitment beneath the particle is independent of CLDN1, while the inhibition of Ezrin signaling, a protein linking plasma membrane receptors to the actin cytoskeleton (20), increases OCLN accumulation beneath HCV particles, promoting virus internalization.

Experimental Procedures

Cell line

Human embryo kidney cells 293T (Hek 293T; ATCC) and cells were cultured in Dulbecco's Modified Eagle's Medium (DMEM) containing 4.5g/L D-Glucose supplemented with 10% fetal bovine serum (FBS; Sigma-Aldrich), 1X Penicillin and streptomycin 5 000 U/mL (Gibco). The hepatocellular carcinoma Huh7.5.1 cells (21) were cultured in DMEM containing 4.5 g/L D-Glucose (Gibco) and 10% FBS (Sigma-Aldrich), 1X MEM non-essential amino acids (Gibco), and 1X gentamicin (10 mg/mL; Gibco).

CRISPR/Cas9 knock-in

Addition of EGFP sequence within the genome of Huh7.5.1 cells was performed using CRISPR/Cas9 gene editing as previously (22, 23). See detailed procedure in Supplementary information.

CRISPR knock-out

The pLenti spCas9 T2A iRFP670 P2A puro plasmid (Addgene #122182) was used as backbone to obtain knock out cells. *Cldn1* gene knock out was performed using the gRNA sequence 5' - gagcgagtcatggccaacgc - 3' under the control of the human U6 promoter and the gRNA sequence 5’ - caacagctgcagccccgcgt - 3’ under the control of the human H1 promoter, both targeting the *cldn1* gene. The cldn1- and *Luc*-targeting constructs are available on Addgene (#166133 and #166134 respectively).

HCVcc production

HCVcc Jc1-Luc and HCVcc Jc1$^{FLAG-E2}$ full length RNA (24-26) were generated from plasmid templates using Megascript T7 transcription kit (Thermo Fisher Scientific) according to the manufacturer’s instructions.

Live cell imaging

Cells were grown on 30 mm diameter #1.5 glass coverslip in 6-well plates for 48 h. Prior imaging, cells were incubated with HCVcc-A594 or HCVcc-A647 in DMEM complete media (Gibco). Image acquisition was performed at 37°C and 5% CO_2 in a dark chamber using an AxioObserver.Z1 inverted microscope (Zeiss) mounted with a spinning disc head (Yokogawa), a back-illuminated EMCCD camera (Evolve, Photometrics) and a 100x, 1.45 NA oil objective (Zeiss) controlled by Visiview v.3.3.0 (Visitron Systems) and MetaMorph (Molecular Devices) software.

Liver slices preparation

All study participants provided informed consent and protocol was approved by the institutional review board. Liver explants were obtained by dissection in sterile conditions. Liver samples were resected away from the tumoral zone, in normal macroscopic area. The donors were not receiving chemotherapy at the time of surgery. Liver explants were transported to the BSL-2 lab in complete William’s medium (0.15% FBS, 1x Insulin-transferrin-selenium, 0.1 µM dexamethasone, 1% essential amino acid, 1% penicillin-streptomycin, 1% glutamax). Liver explants were cut in small cubes (1 cm x 1cm) and placed in 6 well dishes to be fully embedded in 3% low melting point agarose (ThermoFisher Scientific) diluted in PBS. The liver-containing agarose cubes were sliced at a thickness of ≈ 300 µm using a McIlwain tissue chopper, adapted from (27). The slices were collected in cold complete William’s medium and placed in transwells containing a polyester membrane with 0.4 µm pores (Millipore) and cultured for 24 h at air-liquid interface prior infection.

Image analyses

Processing and image quantification were performed using the Fiji version of ImageJ and Bitplane Imaris version 9.2 and 9.7. See details in Supplementary information.

Results

Generation of Huh7.5.1 EGFP-OCLN^{edit} cells

To decipher the spatiotemporal dynamics and role of OCLN during HCV entry, we aimed to obtain a HCV permissive cell line expressing endogenous levels of fluorescent OCLN proteins, as EGFP-OCLN overexpression perturbs its distribution (28). To this end, the genome of Huh7.5.1 cells was edited using a CRISPR/Cas9 knock-in approach as previously described (22, 29, 30). Briefly, cells were transfected with a plasmid coding for the spCas9 protein, a DNA PCR product coding for a guide RNA (gRNA) targeting the ATG region of the *ocln* gene, and an EGFP "donor" plasmid providing the DNA template for homologous recombination (see Figure 1A and Material & Methods for details). Upon sorting and clonal cell selection, a monoclonal Huh7.5.1 EGFP-OCLN^{edit} cell line showed the EGFP sequence inserted on all alleles in the start codon region of the *ocln* gene (Figure 1B). The amount of OCLN protein expressed by wild type or EGFP-OCLN^{edit} Huh7.5.1 cells was measured by western blot (Figure S1A) and flow cytometry (Figure 1C and S1B). As a control for antibody specificity, overexpression of OCLN and analyses of ZO-1 expression levels were also compared. The western blot showed lower amount of EGFP-OCLN, while flow cytometry measurements indicate similar levels of OCLN proteins. This difference can be attributed to technical difficulties to transfer larger proteins from gel to membranes. Similarly, we could not detect significant differences at the mRNA level for OCLN, nor for the other HCV entry factors CLDN1, CD81, and SR-B1 (Figure S1C).

Together, these results show that we successfully added an EGFP in N-terminus of the OCLN protein, at endogenous expression levels and no "ghost" non-fluorescent OCLN remained, two features usually missing when using classic transient transfection.

Functional characterization of Huh7.5.1 EGFP-OCLN^{edit} cells and permissiveness

At the subcellular level, EGFP-OCLN localization was found at TJ cell-cell contact sites, colocalizing with an anti-OCLN antibody staining (Figure S1D), indicating that the EGFP signal correlates with actual OCLN proteins. The wild-type and edited cells exhibited robust polarized features as shown by the staining of the apical marker Ezrin and the upper localization of ZO-1 (Figure 1D and Figure S1E). Of note, in both cell lines, the cells were mostly polarized but patches of non-polarized cells were also observed at lower frequency. To assess whether the relative diffusion of EGFP-OCLN was preserved, fluorescence recovery after photobleaching (FRAP) was performed. We observed that the endogenous EGFP-OCLN proteins were mobile at TJ sites of Huh7.5.1 cells (Figure S2A-C), in a similar fashion to what was observed in MDCK cells under conditions where EGFP-OCLN was overexpressed (31).

Next, we tested whether the EGFP-OCLN protein retained its functional features. Using a transwell system to assess for permeability coefficient as previously done (22, 32), we found that the relative permeability of the wild-type or EGFP-OCLN^{edit} cells did not show significant differences (Figure 1E), indicating that the addition of the EGFP tag does not affect the OCLN's impermeability function. As a control EDTA treatment was impairing the permeability coefficient of both cell lines.

Fifty-percent tissue culture infective dose ($TCID_{50}$) measurement and HCV pseudoparticles (HCVpp) infection assays suggested that the EGFP-OCLN^{edit} cells were less permissive to HCVcc, although it did not reach significance (Figure S3). To further determine whether this decrease was due to the addition of EGFP or to the selected edited clone, we compared permissiveness of these cells using a HCVcc luciferase reporter virus (Jc1-Luc) or VSV-G-expressing pseudoparticles (VSVpp). A slight decrease of permissiveness of the edited cells compared to their wild-type counterpart for both HCVcc and VSVpp was observed (Figure 1F). As VSV is not known to enter in an OCLN-dependent manner, the luciferase activity obtained from HCVcc was normalized by the signal obtained from VSVpp (Figure 1G). In this case, no difference was observed between wild type and EGFP-OCLN edited cells.

HCV-OCLN association occurs out of tight junctions in Huh7.5.1 edited cells

To track HCVcc viral particles in fixed and live samples, we developed a purification and labeling method (see Material & Methods and Figure S4A) based on the recombinant HCVcc Jc1$^{FLAG\text{-}E2}$ (33). Our approach relies on the coupling of the affinity-purified HCVcc particles to A594 or A647 dye through a N-hydroxysuccinimidyl-ester (NHS) reaction. Non-labeled and fluorescently-labeled HCVcc particles showed similar infectivity (Figure S4B-D), indicating that the dyes do not significantly perturb HCV infection.

To determine the localization of HCV particles upon virus-host interactions, kinetic analyses of HCVcc-A647 distribution onto EGFP-OCLN^{edit} edited cells was performed by confocal microscopy (Figure 2A). Fluorescent latex microspheres of 40 nm, a size comparable to HCV virions, were used as controls (Figure 2B). To obtain quantitative information, the virus/microsphere signals were segmented, excluding aggregates, and the presence or absence of OCLN was automatically assessed. The OCLN-positive virus/microsphere, were further classified into two categories: “at TJs” or “out of TJs”. Strikingly, the vast majority of the HCV-OCLN association events occurred out of TJs (Figure 2C-D). Of note, TJ regions are readily recognized by their enriched composition in TJAPs (including OCLN) at intercellular junctions, forming elongated structures along cell-cell contact sites, which can be unambiguously identified on our images. A peak of colocalization was observed at 3 hours post-infection (hpi), which decreases at later time points. Infectious HCV particles requires about 3-4 h to be internalized (Figure S5) highlighting that the timing of maximum HCV-OCLN association correlates with the infectivity assays performed. Quantitative analyses of the number of microspheres at/out of TJs at 3 h post-addition revealed that the beads were not accumulating at TJs (Figure 2B, 2E), similar to observations with HCV. In sharp contrast to HCV particles however, the microspheres outside TJs were not able to accumulate OCLN (Figure 2F), highlighting the specificity of the non-junctional HCV-OCLN association.

We acknowledge that our cell monolayer model does not represent the physiological architecture of a human liver, but we avoided to grow our cells in spheroids to study HCV entry as previously done (18), because such structure seems to behave like a treadmill, sliding-in anything from the outside toward its center. Indeed, we found that Huh7.5.1 fluorescent microspheres incubated with EGFP-OCLN^{edit} spheroids were transported toward the cell center within a few hours, concentrating them in the inner region of the spheroid (Figure S6). This observation suggests that centripetal forces are generated in a non-specific manner in this model and thus, precluding spatiotemporal imaging of HCV-host interactions.

HCV associates with OCLN outside TJs in human liver slices

Whether the incoming HCV particle associate with its entry factor at the TJ or away from it is a recurrent debate, mostly because of the *in vitro* models used to answer this question have unknown physiological relevance. In this context, the *ex vivo* culture of primary human liver slices obtained from excision of adjacent healthy tissues from HBV/HCV/HIV-negative patients likely represent the most physiologically relevant model we could establish. Using an adapted protocol (Figure 3A, Material & Methods and (27)), we cultured healthy organotypic human liver slices (Figure 3B) and infected them 24 h post-slicing with fluorescent HCVcc-A647 virus for 3 h (Figure 3). Upon fixation, permeabilization, labeling and clarification of the tissues, we observed that fluorescent HCV particles were associated to OCLN clusters (Figure 3C-D). Conventional TJs are maintained by a strong F-actin network, as exposed by the phalloidin staining. However, no polymerized actin was found associated to HCV-OCLN clusters, indicating that this interaction occurs in structures that are not part of the TJ belt. Although we never found HCV particles associated to TJs in organotypic human liver slices, we were unable to thoroughly quantify these observations due to the limited number of samples, and this qualitative dataset come as a complement of the quantitative *in vitro* analyses.

Together, our data represents the first observations to our knowledge of HCV interaction with OCLN into human liver at high spatial resolution, allowing us to determine that HCV and OCLN associate in non-TJ structures.

Live imaging highlights increased HCV-OCLN association correlated to decreased virus mobility

To gain more insights onto the role of OCLN in governing HCV' spatiotemporal dynamics at the cell surface, 3D live cell imaging of EGFP-OCLN^{edit} cells incubated for 3 h with HCVcc-A647 was performed using a spinning confocal microscope in BSL-3 environment

(Figure S7 and Movie S1). Single particle tracking of the HCVcc-A647 from the upper plans (surface of the cell) revealed that the virus particles were not directed nor moving toward TJs, further showing that virus sliding is unlikely to represent a *bona fide* HCV entry model in our settings.

Next, we investigated the dynamic properties of single viral particles according to their relative amount of associated OCLN. Spatiotemporal tracking of single particles highlighted that the accumulation of OCLN beneath HCV particles was associated to lower mobility of the complex (Figure 4A-B and Movie S2). A threshold (shown in cyan in Figure 4C) was set based on the mean fluorescence intensity of OCLN, excluding the areas presenting TJs or HCV particles. Automated quantification of the HCV particle speed and its associated OCLN intensity showed a significant inverse correlation between the speed of HCV particles and the OCLN fluorescence intensity (Figure 4C). Comparing the mean speed of HCV particles associated with high levels of OCLN versus HCV particles associated to low/undetectable levels of OCLN confirmed that greater amount of OCLN significantly decreases overall HCV speed (Figure 4D). Beads are devoid of OCLN (Figure 2E-F) and their velocity was slower than HCV particles (Figure 4D). Together, these results suggest that OCLN accumulation stabilizes the virion at the plasma membrane, which could favor internalization.

Single particle tracking allowed to identify the virions that were endocytosed, as shown by the rapid transport of a HCV particle within the cell (Figure 4E, S4 and associated Movies S2-S3). Quantification of these events highlighted that HCV particles located away from TJs were internalized with efficiency greater than 70%, while the particles at TJs or in their vicinity (< 2 µm) were mostly unable to get internalized (Figure 4F). This data reinforces the concept that HCV particles enter cells without the need to slide toward TJs.

Claudin-1 is not required for OCLN recruitment beneath HCV particles

Intrinsically to the experiment, we could see that absence of OCLN at HCV landing site was associated to higher particle mobility (Figure 4A-C) and therefore, we did not perform disruptive OCLN knock-out analyses. Because OCLN is known as the latest component required for HCV entry (10), we thought that knocking out CLDN1, the second-to-last entry factor recruited, should impact OCLN accumulation underneath HCV particles at the plasma membrane. To assess this hypothesis, Huh7.5.1 EGFP-OCLN^{edit} cells were knocked-out for CLDN1 using a CRISPR/Cas9 lentivector expressing two gRNA directed against *cldn1*, a puromycin resistance and an iRFP670 fluorescent protein. A clonal cell line devoid of CLDN1 protein expression was isolated (Figure 5A), which lost permissiveness to HCVcc (Figure 5B). Using the CLDN1 KO Huh7.5.1 cells expressing endogenous EGFP-OCLN^{edit} , we found that HCV particles were still associated with similar levels of non-junctional OCLN at the plasma membrane (Figure 5C-E), indicating that CLDN1 appears not to be required for OCLN recruitment, although it is important for permissiveness.

Ezrin phosphorylation is required for OCLN-HCV association and internalization outside TJs

Because targeting a HCV entry factor supposedly acting right before OCLN did not prevent OCLN recruitment, we seek to identify other cellular partners involved in OCLN recruitment in order to better characterize the role of OCLN clustering beneath HCV particles. The Ezrin-Radixin-Moesin (ERM) complex is a plasma membrane/cytoskeleton linkage through interactions between cytosolic tails of transmembrane receptors and the actin network (20). Ezrin has been shown to be necessary for successful HCV entry (34), although the mechanism of action remains unknown. Thus, we investigated whether Ezrin could play a role in OCLN accumulation beneath HCV particles. However, because Ezrin is involved in numerous processes, including TJ formation, we did not silence the protein to preserve TJ structures. Instead, we used the small molecule NSC668394 that prevents Ezrin phosphorylation in an acute, yet reversible manner (35). We observed that the Ezrin inhibitor (Ez. Inh) does not impact TJ structures once they are formed, nor the cell polarity (Figure 6A). Consistently, the permeability coefficient of cells treated with the compound was similar to untreated control cells (Figure 6B). Moreover, Ez. Inh had no significant impact on the expression of the HCV entry factors SR-B1, CLDN1 and CD81 at the cell surface (Figure 6C-D). Although the presence of Ezrin was shown to be necessary for HCV infection (34), whether acutely preventing Ezrin phosphorylation would inhibit HCV infection was unknown. Using Huh7.5.1 EGFP-OCLN^{edit} cells infected with HCVcc in the presence or the absence of the Ez. Inh, we found that preventing Ezrin phosphorylation is sufficient to prevent HCV infection (Figure 6E). Of note, the relatively high doses used are consistent with the effective concentration reported for this compound (35).

Evaluation of the impact of Ez. Inh on HCV entry showed that virus attachment was decreased (Figure 6F). In contrast, the particles that managed to attach to the cell surface were recruiting more OCLN in the presence of the inhibitor (Figure 6G). In this context of Ez. Inh-induced OCLN accumulation, the HCV particles bound to the cell surface were very efficiently endocytosed (Figure 6H), suggesting that the accumulation of OCLN beneath the particle participates in successful HCV internalization.

Discussion

In this study, we investigated the spatiotemporal dynamics of HCV in association with one of its main entry factors: OCLN. To this end, we generated a novel CRISPR/Cas9 bioengineered Huh7.5.1 cell line expressing endogenous levels of fluorescent OCLN and performed high-resolution 3D live cell imaging. Our observations indicated that the virions were not trafficking toward the TJs. In contrast, HCV particles were accumulating OCLN proteins away from TJs as observed both *in vitro* and in *ex vivo* organotypic cultures of human liver slices.

Live cell imaging of viral receptors is difficult to perform because the fluorescent tagging of the receptor is usually performed by cDNA transfection, therefore inducing overexpression of the receptor and the reminiscence of non-tagged, endogenous receptors. In the case of OCLN, transient transfection of its cDNA causes OCLN mislocalization (28), and thus, this approach is not suited for the study of HCV entry. Here, we took advantage of the CRISPR/Cas9 technique (30) to insert a fluorescent tag within the genome of the permissive Huh7.5.1 cells. Our extensive characterization of these cells showed that they retained similar features as their parental non-edited lineage, including permissiveness to HCVcc infection. Of note, tagging the CLDN1 entry factor using the same CRISPR-based approach led the cells to be fully resistant to the infection (22). Together, the Huh7.5.1 EGFP-OCLN^{edit} cells represent a functional tool to interrogate for OCLN distribution over time as well as a reporter cell line for OCLN expression level variation.

Our assay showed that HCV was not sliding toward TJs, and surprisingly, we found that instead, OCLN was recruited outside TJs to meet with the virus. Consistent with our findings, recent work by Lavie *et al.* found that TJ localization of OCLN is not a prerequisite for HCV infection in polarized hepatocytes (19). At this stage however, we do not know how HCV captures the OCLN proteins. One could assume that low amount of OCLN proteins diffusing at the plasma membrane may be captured by the complex formed by HCV with upstream entry factors following models previously proposed for other viruses (15). This could well explain why HCV virions take a relatively long time to get internalized (3-4 h; Figure S5).

The main drawback of our model resides in the fact that the cells are grown as 2D monolayers, therefore exposing their apical side to the virus, a topology that is opposed to physiological conditions where hepatocytes expose their basolateral side to the bloodstream where the virus comes from. Recently, Huh7.5 cells were grown in 3D, exposing the basolateral side of the cells (18). The authors proposed that HCV virions tend to slide to the center of the cell mass where OCLN and other TJ-associated proteins were found. Nano-objects tend to naturally move toward the center of organoids due to a treadmilling effect (36), and this is also what we could observe in our hands using microspheres (Figure S6).

As all these models have specific drawbacks, we developed organotypic cultures of human liver explants, which may be considered the most physiologically relevant model to study HCV-receptor interactions at high-resolution. This model has the advantage to exhibit complex multicellular 3D cytoarchitecture of the hepatic macro- and micro-environment, ideally suited to gain relevant mechanistic insights into liver diseases, including viral hepatitis, while allowing genetic manipulation (37). This *ex vivo* model was previously reported to be relevant to study HCV infection (27), an approach that we adapted here.

Beyond the specific localization of HCV-OCLN association, our gene edited cells allowed us to monitor in real time and at endogenous levels the dynamics of this association at high spatiotemporal resolution. The quantitative analysis of virus movement at the cell surface and the progressive accumulation of OCLN beneath the virus cannot be done in 3D models (organoids or *ex vivo* liver explant). Numerous considerations have to be taken into accounts for live cell imaging of viruses, and technical challenges, such as objective's working distance, light penetration depth and refractive index of non-cleared tissues need to be overcome as recently reviewed (38, 39).

Although OCLN is essential for post-attachment entry events of HCV particles, its exact role is not clear (19, 40). OCLN is a post-binding entry factor that has been suggested to bridge the virion to intracellular dynamin2, favoring internalization (11, 41). However, dynamin2 is mostly recruited at late stages of clathrin-coated pits and thus, does not fully explain how HCV OCLN can induce HCV endocytosis. Here we describe for the first time that OCLN recruitment correlates with HCV particle stabilization at the plasma membrane, a mechanism employed by viruses to be efficiently internalized (15). Indeed, clustering viral receptors for efficient internalization is a relevant concept that has previously been demonstrated for other viruses, including the human immunodeficiency virus (HIV), dengue virus (DENV), transmissible gastroenteritis virus (TGEV) and the canine parvovirus (CPV) (42-45). Interestingly, while HCV is probably one of the viruses to which the greatest number of entry factors has been attributed to, very little is known about HCV-receptor dynamics. Here, we show for the first time the spatiotemporal dynamics of HCV-OCLN association and discovered that accumulation of non-junctional OCLN beneath HCV particles slows down the mobility of virions at the plasma membrane, which in turn could favor virus internalization and infection.

In the hierarchy of HCV entry factors, it is believed that SR-B1 and CD81 participate in the firm attachment of HCV particles, followed by engagement of CLDN1 upon non-junctional interaction with CD81, while OCLN arrives the latest to complete the HCV entry process (6, 10). Unexpectedly, we found that CLDN1 was not required for OCLN accumulation at the virion's attachment site, although it is essential for efficient HCV infection. The molecular mechanism responsible for OCLN recruitment remains unknown, but we could show that it was independent of CLDN1 expression.

Clustering of receptors implies that protein-protein interactions and/or restricted microdomains form at the cell surface. Because OCLN has been shown to cis-oligomerize (46), it is possible that the recruitment of a single OCLN protein beneath an HCV particle initiates subsequent OCLN accumulation through *cis* OCLN-OCLN interactions. In this scenario, lateral OCLN diffusion at the plasma membrane would occur, and although our imaging approach cannot detect single molecule diffusion, further work, using for instance fluorescence correlative spectroscopy, could shed light on this process. Alternatively, microdomains at the cell surface could form through actin-dependent compartmentalization.

Because the ERM proteins link transmembrane integral proteins at the plasma membrane to the actin cytoskeleton (20), they could participate in OCLN clustering at the cell surface. The Ezrin protein is essential for HCV infection (34), but its mechanism of action remains unknown. By using a small molecule inhibiting Ezrin phosphorylation in an acute manner, we found that it was able to inhibit HCV infection while maintaining TJ integrity (Figure 4D-F). CD81 mediates virus attachment (13, 14) and its stimulation has been shown to induce Ezrin phosphorylation (47). Because we showed that inhibition of Ezrin phosphorylation decreases virus binding (Figure 4G), it is likely that the phosphorylation of Ezrin is required to strengthen virus binding to the cell surface. The viral particles that nevertheless succeeded to attach to the cell surface were significantly more efficient in recruiting OCLN (Figure 4H). One can speculate that inhibiting the function of Ezrin increases transmembrane protein diffusion at the cell surface, which in turn could increase the chances for HCV to meet with its entry factors.

The increased OCLN accumulation beneath the virions was associated with very efficient particle internalization (Figure 4I), indicating that a certain threshold of OCLN may be required for HCV internalization. Previous links have been established between OCLN and Ezrin phosphorylation (48, 49), but further studies will be required to fully elucidate the complex series of events leading to efficient HCV internalization.

In conclusion, our study demonstrated that HCV entry at the cell surface occurs away from TJs. We also provided the spatiotemporal landscape of HCV-OCLN association and explored the complex interplay with other host factors involved in HCV entry. While future studies should aim at combining multi-receptor co-imaging in physiologically relevant context, our high-resolution imaging coupled to physiological infection models allowed us to solve longstanding questions in the field and provide broader insights about virus entry dynamics.

Acknowledgments

We thank Dr. Pablo Gastaminza for kindly sharing data on HCV infection kinetics and Drs. Ralf Bartenschlager, Frank Chisari, Takaji Wakita and Charles M. Rice for the gift of viral strains and cell lines. We would like to acknowledge the MRI imaging facility for advice and training. The spinning disk image acquisitions in BSL-3 environment were performed at CEMIPAI (UAR3725 CNRS, Montpellier University). This work benefited from equipment of the CRB-CHUM facility of the CHU de Montpellier (http://www.chu-montpellier.fr), Biobanque identifier: BB-0033-00031. **Funding**: ATIP-AVENIR starting grant (RG); INSERM and the Region Grand-Est salary support (CMHC); EMBO Long Term Fellowship grant EMBO ALTF 1428-2016 (CMD); People Program (Marie Curie Actions) of the European Union's Seventh Framework Program FP7/2007-2013 under REA grant agreement n° PCOFUND-GA-2013-609102, through the PRESTIGE program coordinated by Campus France (NVAN); The French Agency for Research on AIDS and Viral Hepatitis (ANRS) salary support (MSD, NVAN); Institut Universitaire de France (IUF) support (YM) ; ERC Advanced grant HEPCIR agreement N° 667273 (TFB).

Author Contributions

Conceptualization: RG
Methodology: MSD, CMHC, CMD, EP, YB, OF, NVAN, PR, VL, RG
Investigation: MSD, CMHC, CMD, YB, RG
Resources: BR, TFB
Supervision: YM, RG
Visualization: MSD, CMHC, RG
Writing—original draft: RG
Writing—review & editing: MSD, RG

Competing Interest

The authors declare that they have no competing interests.

References

1. H. Sung *et al.*, Global Cancer Statistics 2020: GLOBOCAN Estimates of Incidence and Mortality Worldwide for 36 Cancers in 185 Countries. *CA Cancer J Clin* **71**, 209-249 (2021).

2. M. Sanduzzi-Zamparelli, L. Boix, C. Leal, M. Reig, Hepatocellular Carcinoma Recurrence in HCV Patients Treated with Direct Antiviral Agents. *Viruses* **11** (2019).
3. E. Blanchard *et al.*, Hepatitis C virus entry depends on clathrin-mediated endocytosis. *Journal of virology* **80**, 6964-6972 (2006).
4. K. E. Coller *et al.*, RNA interference and single particle tracking analysis of hepatitis C virus endocytosis. *PLoS pathogens* **5**, e1000702 (2009).
5. B. D. Lindenbach, C. M. Rice, The ins and outs of hepatitis C virus entry and assembly. *Nature reviews. Microbiology* **11**, 688-700 (2013).
6. M. B. Zeisel, D. J. Felmlee, T. F. Baumert, Hepatitis C virus entry. *Current topics in microbiology and immunology* **369**, 87-112 (2013).
7. J. Dubuisson, F. L. Cosset, Virology and cell biology of the hepatitis C virus life cycle: an update. *Journal of hepatology* **61**, S3-S13 (2014).
8. D. Du *et al.*, The tight junction protein, occludin, regulates the directional migration of epithelial cells. *Dev Cell* **18**, 52-63 (2010).
9. P. M. Cummins, Occludin: one protein, many forms. *Mol Cell Biol* **32**, 242-250 (2012).
10. M. Sourisseau *et al.*, Temporal analysis of hepatitis C virus cell entry with occludin directed blocking antibodies. *PLoS Pathog* **9**, e1003244 (2013).
11. I. Benedicto *et al.*, The tight junction-associated protein occludin is required for a postbinding step in hepatitis C virus entry and infection. *J Virol* **83**, 8012-8020 (2009).
12. A. Ploss *et al.*, Human occludin is a hepatitis C virus entry factor required for infection of mouse cells. *Nature* **457**, 882-886 (2009).
13. H. J. Harris *et al.*, Claudin association with CD81 defines hepatitis C virus entry. *The Journal of biological chemistry* **285**, 21092-21102 (2010).
14. E. G. Cormier *et al.*, CD81 is an entry coreceptor for hepatitis C virus. *Proceedings of the National Academy of Sciences of the United States of America* **101**, 7270-7274 (2004).
15. S. Boulant, M. Stanifer, P. Y. Lozach, Dynamics of virus-receptor interactions in virus binding, signaling, and endocytosis. *Viruses* **7**, 2794-2815 (2015).
16. R. Bartenschlager, V. Lohmann, F. Penin, The molecular and structural basis of advanced antiviral therapy for hepatitis C virus infection. *Nature reviews. Microbiology* **11**, 482-496 (2013).
17. C. B. Coyne, J. M. Bergelson, Virus-induced Abl and Fyn kinase signals permit coxsackievirus entry through epithelial tight junctions. *Cell* **124**, 119-131 (2006).
18. Y. Baktash, A. Madhav, K. E. Coller, G. Randall, Single Particle Imaging of Polarized Hepatoma Organoids upon Hepatitis C Virus Infection Reveals an Ordered and Sequential Entry Process. *Cell host & microbe* **23**, 382-394 e385 (2018).
19. M. Lavie *et al.*, Role of the cytosolic domain of occludin in trafficking and hepatitis C virus infection. *Traffic* **20**, 753-773 (2019).
20. O. Maniti, K. Carvalho, C. Picart, Model membranes to shed light on the biochemical and physical properties of ezrin/radixin/moesin. *Biochimie* **95**, 3-11 (2013).
21. J. Zhong *et al.*, Robust hepatitis C virus infection in vitro. *Proc Natl Acad Sci U S A* **102**, 9294-9299 (2005).
22. C. M. H. Clement *et al.*, Characterisation of endogenous Claudin-1 expression, motility and susceptibility to hepatitis C virus in CRISPR knock-in cells. *Biol Cell* **112**, 140-151 (2020).
23. M. S. Deffieu *et al.*, Rab7-harboring vesicles are carriers of the transferrin receptor through the biosynthetic secretory pathway. *Sci Adv* **7** (2021).

24. T. Wakita *et al.*, Production of infectious hepatitis C virus in tissue culture from a cloned viral genome. *Nature medicine* **11**, 791-796 (2005).
25. A. Merz *et al.*, Biochemical and morphological properties of hepatitis C virus particles and determination of their lipidome. *The Journal of biological chemistry* **286**, 3018-3032 (2011).
26. T. Pietschmann *et al.*, Construction and characterization of infectious intragenotypic and intergenotypic hepatitis C virus chimeras. *Proceedings of the National Academy of Sciences of the United States of America* **103**, 7408-7413 (2006).
27. S. Lagaye *et al.*, Efficient replication of primary or culture hepatitis C virus isolates in human liver slices: a relevant ex vivo model of liver infection. *Hepatology* **56**, 861-872 (2012).
28. M. Furuse, K. Fujimoto, N. Sato, T. Hirase, S. Tsukita, Overexpression of occludin, a tight junction-associated integral membrane protein, induces the formation of intracellular multilamellar bodies bearing tight junction-like structures. *Journal of cell science* **109 (Pt 2)**, 429-435 (1996).
29. Y. Y. Chou *et al.*, Identification and characterization of a novel broad spectrum virus entry inhibitor. *Journal of virology* 10.1128/JVI.00103-16 (2016).
30. F. A. Ran *et al.*, Genome engineering using the CRISPR-Cas9 system. *Nature protocols* **8**, 2281-2308 (2013).
31. L. Shen, C. R. Weber, J. R. Turner, The tight junction protein complex undergoes rapid and continuous molecular remodeling at steady state. *The Journal of cell biology* **181**, 683-695 (2008).
32. N. V. Ayala-Nunez *et al.*, Zika virus enhances monocyte adhesion and transmigration favoring viral dissemination to neural cells. *Nature communications* **10**, 4430 (2019).
33. M. T. Catanese *et al.*, Ultrastructural analysis of hepatitis C virus particles. *Proceedings of the National Academy of Sciences of the United States of America* **110**, 9505-9510 (2013).
34. T. N. Bukong, K. Kodys, G. Szabo, Human ezrin-moesin-radixin proteins modulate hepatitis C virus infection. *Hepatology* **58**, 1569-1579 (2013).
35. G. Bulut *et al.*, Small molecule inhibitors of ezrin inhibit the invasive phenotype of osteosarcoma cells. *Oncogene* **31**, 269-281 (2012).
36. Y. Gao *et al.*, Predictive models of diffusive nanoparticle transport in 3-dimensional tumor cell spheroids. *AAPS J* **15**, 816-831 (2013).
37. E. Palma, E. J. Doornebal, S. Chokshi, Precision-cut liver slices: a versatile tool to advance liver research. *Hepatology international* **13**, 51-57 (2019).
38. M. S. Deffieu, R. Gaudin, Imaging the Hepatitis B Virus: Broadcasting Live. *Trends Microbiol* **27**, 810-813 (2019).
39. W. C. Lemon, K. McDole, Live-cell imaging in the era of too many microscopes. *Current opinion in cell biology* **66**, 34-42 (2020).
40. Q. Ding, M. von Schaewen, A. Ploss, The impact of hepatitis C virus entry on viral tropism. *Cell host & microbe* **16**, 562-568 (2014).
41. S. Liu *et al.*, The second extracellular loop dictates Occludin-mediated HCV entry. *Virology* **407**, 160-170 (2010).
42. Y. Yuan *et al.*, Single-Molecule Super-Resolution Imaging of T-Cell Plasma Membrane CD4 Redistribution upon HIV-1 Binding. *Viruses* **13** (2021).

43. O. Dejarnac *et al.*, TIM-1 Ubiquitination Mediates Dengue Virus Entry. *Cell Rep* **23**, 1779-1793 (2018).
44. D. K. Cureton, C. E. Harbison, E. Cocucci, C. R. Parrish, T. Kirchhausen, Limited transferrin receptor clustering allows rapid diffusion of canine parvovirus into clathrin endocytic structures. *Journal of virology* **86**, 5330-5340 (2012).
45. J. Wang, Y. Li, S. Wang, F. Liu, Dynamics of transmissible gastroenteritis virus internalization unraveled by single-virus tracking in live cells. *FASEB journal : official publication of the Federation of American Societies for Experimental Biology* **34**, 4653-4669 (2020).
46. J. Cording *et al.*, In tight junctions, claudins regulate the interactions between occludin, tricellulin and marvelD3, which, inversely, modulate claudin oligomerization. *Journal of cell science* **126**, 554-564 (2013).
47. G. P. Coffey *et al.*, Engagement of CD81 induces ezrin tyrosine phosphorylation and its cellular redistribution with filamentous actin. *Journal of cell science* **122**, 3137-3144 (2009).
48. M. Murata *et al.*, Occludin induces microvillus formation via phosphorylation of ezrin in a mouse hepatic cell line. *Experimental cell research* **366**, 172-180 (2018).
49. C. Decaens, D. Cassio, Spatiotemporal expression of catenins, ZO-1, and occludin during early polarization of hepatic WIF-B9 cells. *American journal of physiology. Cell physiology* **280**, C527-539 (2001).

Figures

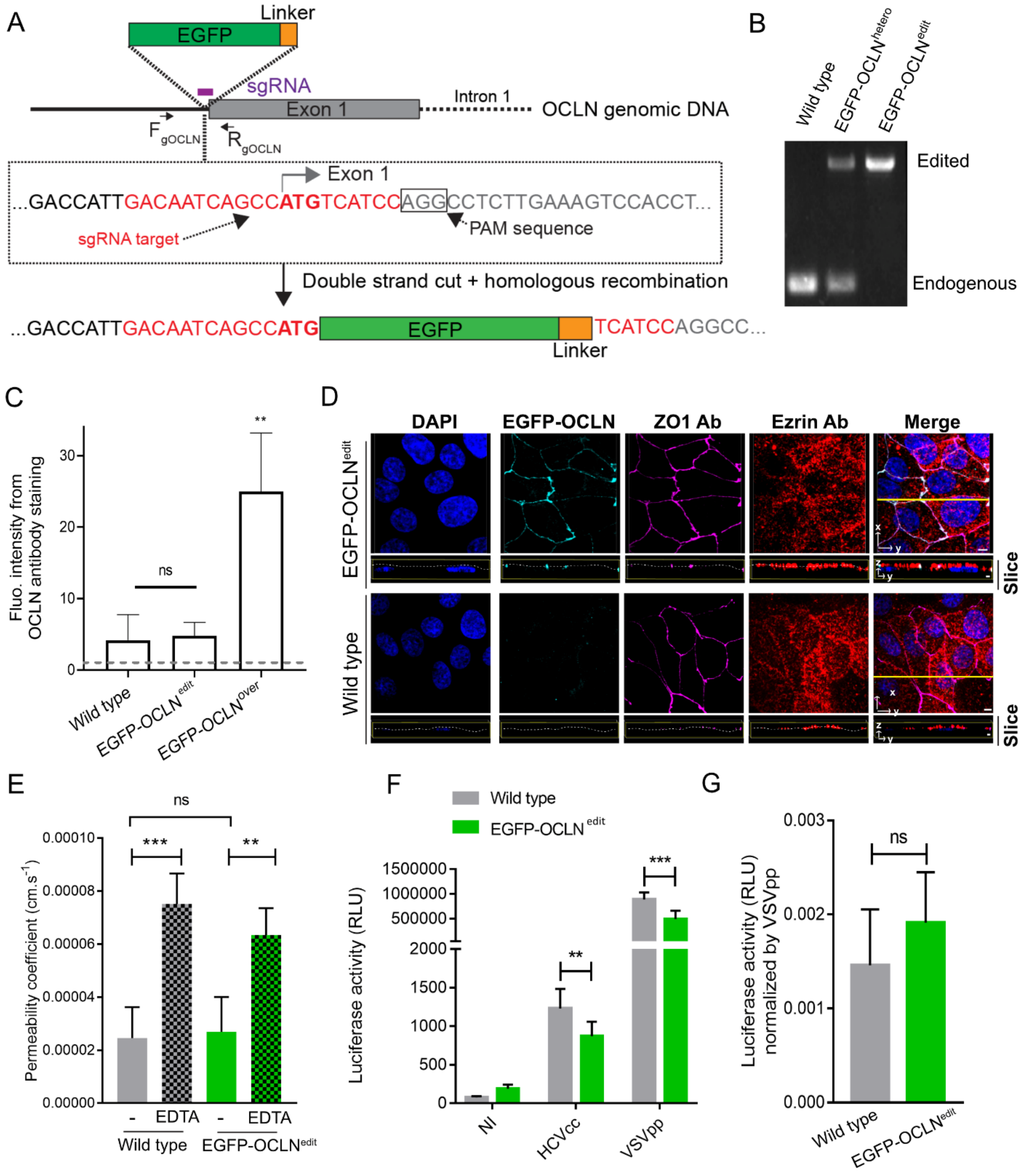

Figure 1

Figure 1. Generation and characterization of Huh7.5.1 EGFP-OCLN^{edit} edited cells. (**A**) Scheme describing the targeting of *ocln* gene with the assistance of site-specific CRISPR/Cas9 endonuclease. The gRNA (violet) was designed to overlap the ATG start

codon (bold red) of the *ocln* gene to allow Cas9-dependent double-strand cut. The EGFP-linker sequence (green-orange) is shown upon homologous recombination in the context of the *ocln* gene. (**B**) The genomic DNA of clonal Huh7.5.1 cell lines was extracted and PCR using the F_{gOCLN} and R_{gOCLN} primers (see arrows in **A**). The non-edited *ocln* gene (endogenous) is seen as a lower band, while upper bands correspond to the EGFP sequence inserted into the ATG region of *ocln* (edited). (**C**) Huh7.5.1 cells overexpressing EGFP-OCLN or endogenously edited for EGFP-OCLN^{edit} expression were fixed and stained with rabbit anti-OCLN antibody and the secondary antibody anti-rabbit A647. The bar graph indicates the mean fluorescence intensity of OCLN in the different conditions. Background staining was represented as a grey dash bar and corresponds to cells labeled with secondary antibody alone. 10 000 cells were counted in triplicate conditions. The graph shows the means +/- SD from two independent experiments. Two-tailed p value was non-significant (ns) or < 0.01 (**). (**D**) EGFP-OCLN^{edit} (cyan) cells and wild type cells were fixed, permeabilized and stained using antibodies against ZO1 (magenta) and Ezrin (red), and Dapi (Blue) and 3D spinning disk confocal microscopy was performed. The images represent the top view of a 3D reconstruction and the lower panels correspond to the orthogonal YZ slice extracted at the yellow line. XY scale bar = 10 µM. YZ scale bar = 5 µM. (**E**) Wild type or edited Huh7.5.1 cells were seeded on transwell inserts with 0.4 µm pores for 4 days. The media of the upper chamber in which the cells were grown was replaced by media containing 50 µM of Lucifer yellow and the permeability coefficient was assessed by measuring the Lucifer Yellow fluorescence intensity in the lower chamber 2 h post-incubation (see Methods for details). EDTA was used as a positive control. The bar graph corresponds to the mean +/- SD from three experiments performed in duplicates. Two-tailed p value was non-significant (ns) or < 0.01 (**) or < 0.001 (***). (**F**) Wild type and EGFP-OCLN^{edit} cells were inoculated with the luciferase reporter viruses Jc1-Luc strain (HCVcc) or VSV-G pseudoparticles (VSVpp). Luminescence was measured at 72 h post-infection. RLU: Relative luminometer units. The bar graph corresponds to the mean +/- SD from three experiments performed in triplicates. Two-tailed p value was < 0.01 (**) or < 0.001 (***). (**G**) The data for HCVcc shown in **F** were normalized for each cell line by the value obtained from the VSVpp infection. ns: non-significant.

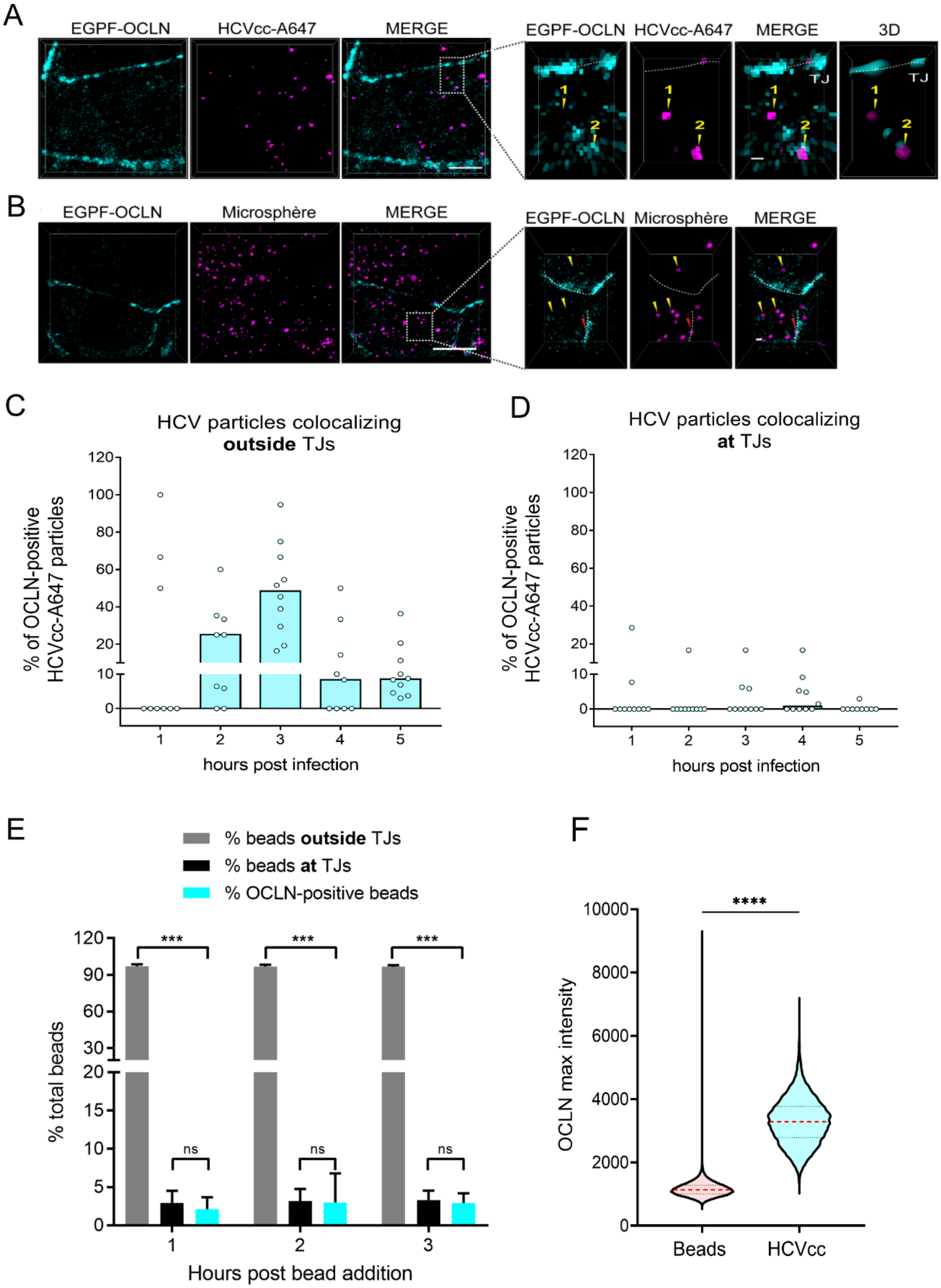
A
EGPF-OCLN
HCVcc-A647
MERGE
EGPF-OCLN
HCVcc-A647
MERGE
3D
1
2
TJ
B
EGPF-OCLN
Microsphère
MERGE
EGPF-OCLN
Microsphère
MERGE
C
HCV particles colocalizing outside TJs
% of OCLN-positive HCVcc-A647 particles
120
100
80
60
40
20
10
0
1
2
3
4
5
hours post infection
D
HCV particles colocalizing at TJs
% of OCLN-positive HCVcc-A647 particles
120
100
80
60
40
20
10
0
1
2
3
4
5
hours post infection
E
% beads outside TJs
% beads at TJs
% OCLN-positive beads
120
90
60
30
20
15
10
5
0
% total beads
***
***
***
ns
ns
ns
1
2
3
Hours post bead addition
F
****
10000
8000
6000
4000
2000
0
OCLN max intensity
Beads
HCVcc

Figure 2

Figure 2. Quantification of OCLN-positive HCV particles upon infection. Huh7.5.1 EGFP-OCLN^{edit} cells were grown on coverslips, incubated with HCVcc-A647 and fixed at indicated time post infection and mounted in Dapi-fluoromount for confocal imaging. (**A**) Representative 3D confocal images (top view) of EGFP-OCLN^{edit} (cyan) and HCVcc-A647 (magenta) acquired from cells infected for 5 h. Scale bar = 5 µm. The yellow arrows highlight two HCVcc particles at the surface of the cell, arrow 2 colocalizing with OCLN signal. The white dotted line shows the position of the TJ. (**B**) Representative 3D confocal images (top view) of EGFP-OCLN^{edit} edited cells (cyan) incubated for 3 h with microspheres (magenta). Scale bar = 5 µm. The yellow arrows highlight microspheres at the surface of the cell. The red arrow points at a microsphere colocalizing with OCLN signal at TJs. The white dotted line indicates the position of the TJ. (**C-D**) The bar graph shows the percentage of HCVcc-A647 particles OCLN-positive colocalizing outside (**C**) or at (**D**) TJs at indicated time post-infection quantified using ImageJ. Each dot corresponds to a field of view. n = 9-10 field per time point. (**E**) The bar graph shows the percentage of microsphere localizing outside TJs (grey bar), at TJs (black bar) or colocalizing with OCLN (cyan bar) at indicated time post microsphere addition. n = 10 fields of view per time point. (**F**) The distribution graph represents the maximum intensity of EGFP-OCLN measured under HCVcc-AF594 particles (HCVcc) or microsphere (Beads) tracked over time. Each intensity value was extracted from all time points and tracks from at least three individual movies for each condition. Movies were carried out at an interval of 15 sec for 45 min. Two-tailed p value was < 0.005 (***) or < 0.001 (****).

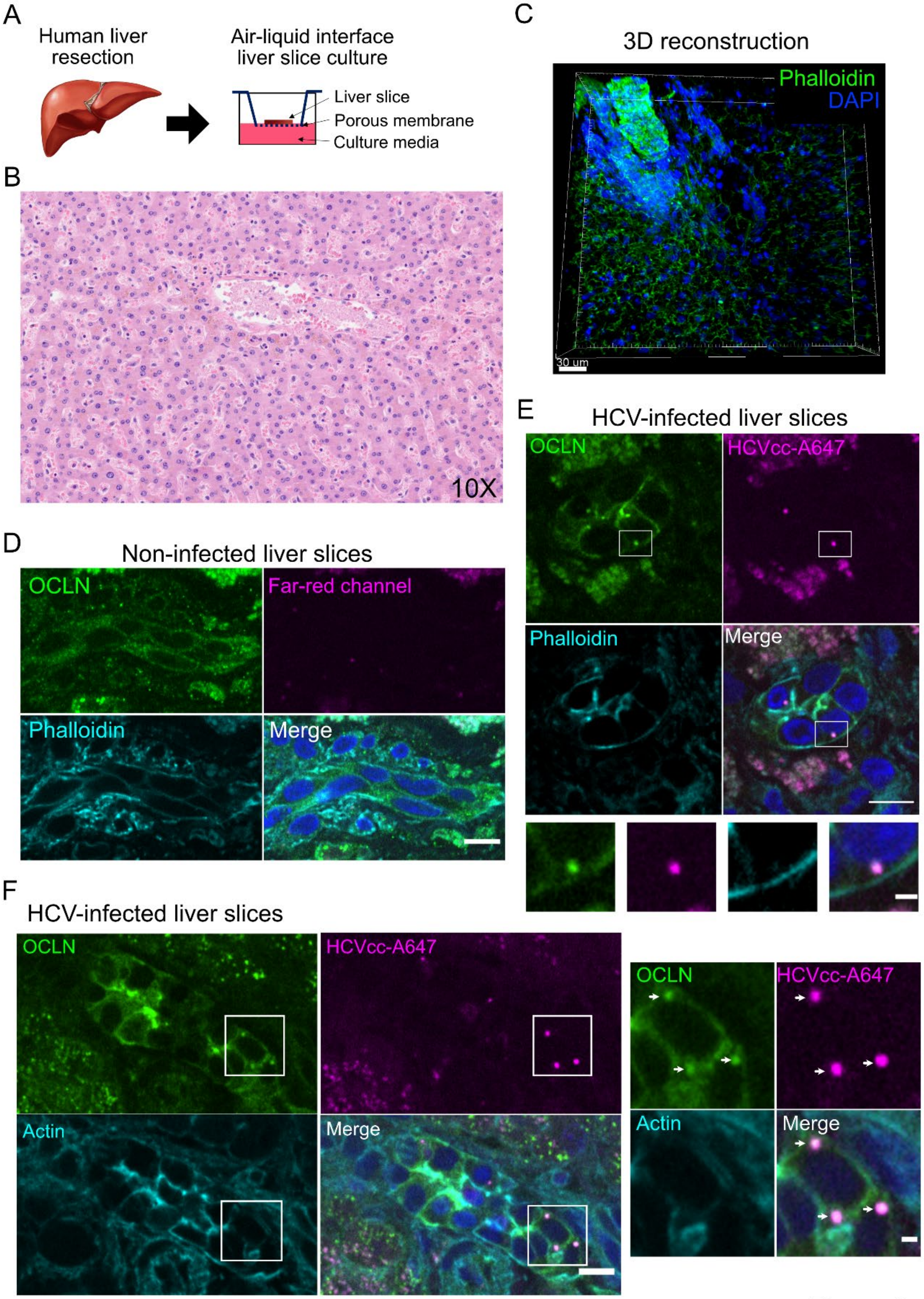
A
Human liver resection
Air-liquid interface liver slice culture
Liver slice
Porous membrane
Culture media
B
10X
C
3D reconstruction
Phalloidin
DAPI
30 um
D
Non-infected liver slices
OCLN
Far-red channel
Phalloidin
Merge
E
HCV-infected liver slices
OCLN
HCVcc-A647
Phalloidin
Merge
F
HCV-infected liver slices
OCLN
HCVcc-A647
Actin
Merge
OCLN
HCVcc-A647
Actin
Merge

Figure 3

Figure 3. Interaction between HCVcc-A647 and OCLN in human liver slices. (**A**) Scheme representing the liver slicing procedure and culture maintenance. Human liver resection was sliced at 300 μm using a tissue chopper. Slices were then placed in transwells at air-liquid interface. (**B**) Liver histology for observation of liver integrity using Haematoxylin & Eosin staining. (**C**) Three-dimensional views of two liver slices, imaged by spinning disk confocal microcopy. Staining represents phalloidin-488 (actin, green) and DAPI (nuclei, blue). Scale bar = 30 μm. Images were taken from two different donors. (**D**) Representative z-stack image from uninfected liver slices were processed by spinning disk confocal microscopy. Liver slices were stained using an anti-OCLN antibody (green), phalloidin-488 (actin, cyan) and DAPI (nuclei, blue). Far red channel was used as a background control for the absence of HCV-cc A647 particles. Scale bar = 10 μm. (**E-F**) The micrographs represent immunofluorescence from a human liver slice infected for 3 h with HCVcc-A647 (magenta) and stained using an anti-OCLN antibody (green), phalloidin-488 (Actin, cyan) and DAPI (nuclei, blue). The white squares represent the region of co-distribution between HCVcc-A647 and OCLN. Scale bar = 10 μm. The insets represent magnified views from the white squares representing OCLN co-distributing with HCVcc-647 (white arrows) out of tight junctions. Scale bar = 2 μm.

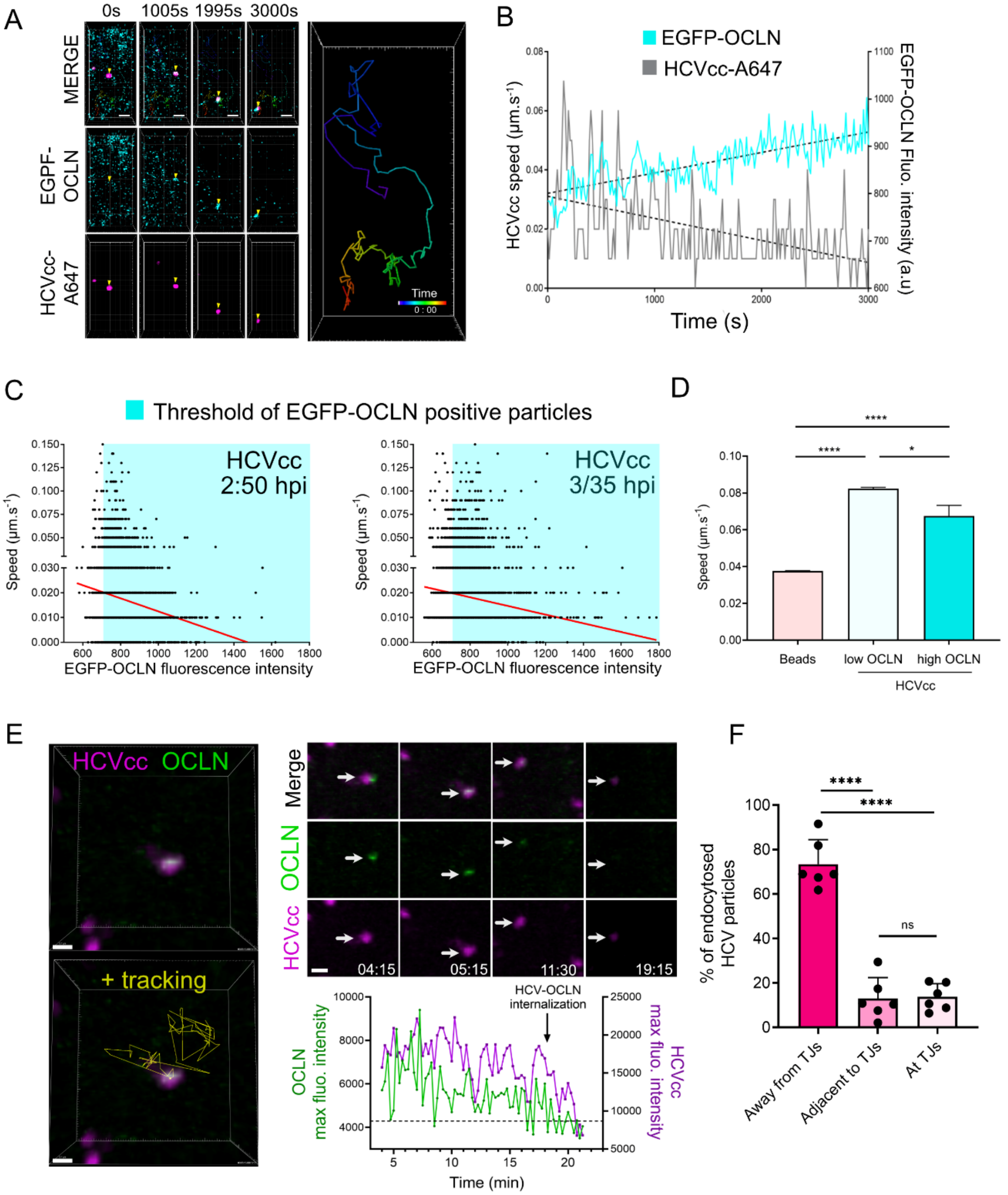

Figure 4

Figure 4. Dynamics and role of OCLN during HCV entry. (**A-C**) Huh7.5.1 EGFP-OCLN^{edit} cells were incubated with HCVcc-A647 for 1 to 5 h prior imaging using a spinning disc confocal microscope. Three-dimensional images were acquired every 15 s for 30-45 min. (**A**) The left panels (and associated Movie S2) show a top view of a 3D stack from a cropped time-lapse series in which the EGFP-OCLN (cyan) and HCVcc-A647 (magenta) signals were merged. The yellow arrowheads highlight a single HCV particle colocalizing

with OCLN. The right panel depicts the color-coded tracked movement of the HCV particle overtime. No recruitment of HCV particles to the TJs could be observed. Scale bar = 5 µM. (**B**) The graph shows the fluorescence intensity of OCLN (cyan, right axis) and the associated speed of the HCV particle (grey, left axis) as a function of time. (**C**) The dot plots show a statistically significant inverse correlation between the speed of the HCV particles at each time as a function of the relative fluorescence intensity of EGFP-OCLN. The red line corresponds to the linear regression curve. Left panel 2:50 hpi; right panel 3:35 hpi. n = 6 movies per condition. Pearson correlation coefficient < 0.001. (**D**) The bar graph represents the speed (µm/s) of HCVcc-AF594 particles (HCVcc) or fluorescent microspheres (Beads) in presence or absence of OCLN. High OCLN corresponds to HCVcc particles exhibiting maximum fluorescence intensity of OCLN > 5000 a.u under the particle while low OCLN corresponds to intensity values < 5000 a.u. Data represents n > 210 OCLN fluorescence intensity objects from 3 individual movies for each condition. (**E**) Representative images extracted from Movie S3 showing 3D visualization of HCVcc-A594 particle (magenta) co-distributed with a cluster of EGFP-OCLN (green) tracked over time (yellow line) in the left panel. The right panels are cropped time-lapse series extracted from Movie S3. Scale bars = 0.7 µm. The graph represents the tracking of the maximum fluorescence intensities of HCVcc-A594 (magenta) and EGFP-OCLN (green) over time. The arrow shows the time at which internalization of HCV-OCLN get internalized within the cell. The dotted line signifies fluorescence background. (**F**) The bar graph represents the localization of endocytosed HCVcc particles related to TJs. Tracks were extracted from 6 different movies obtained from two independent experiments. The decrease in the mean intensity of HCVcc particle over time was used to identify internalization events. The events were classified according to their distance to EGFP-OCLN TJs. Away from TJ > 2 µm, 0 µm < adjacent to TJ > 2 µm, at TJ = 0 µm. Movies were performed at an interval of 15 sec for 45 min. n = 372 events. The graph shows means from six movies +/- SEM. Two-tailed p value was < 0.05 (*), < 0.01 (**), < 0.005 (***) or < 0.001 (****), ns = non-significant.

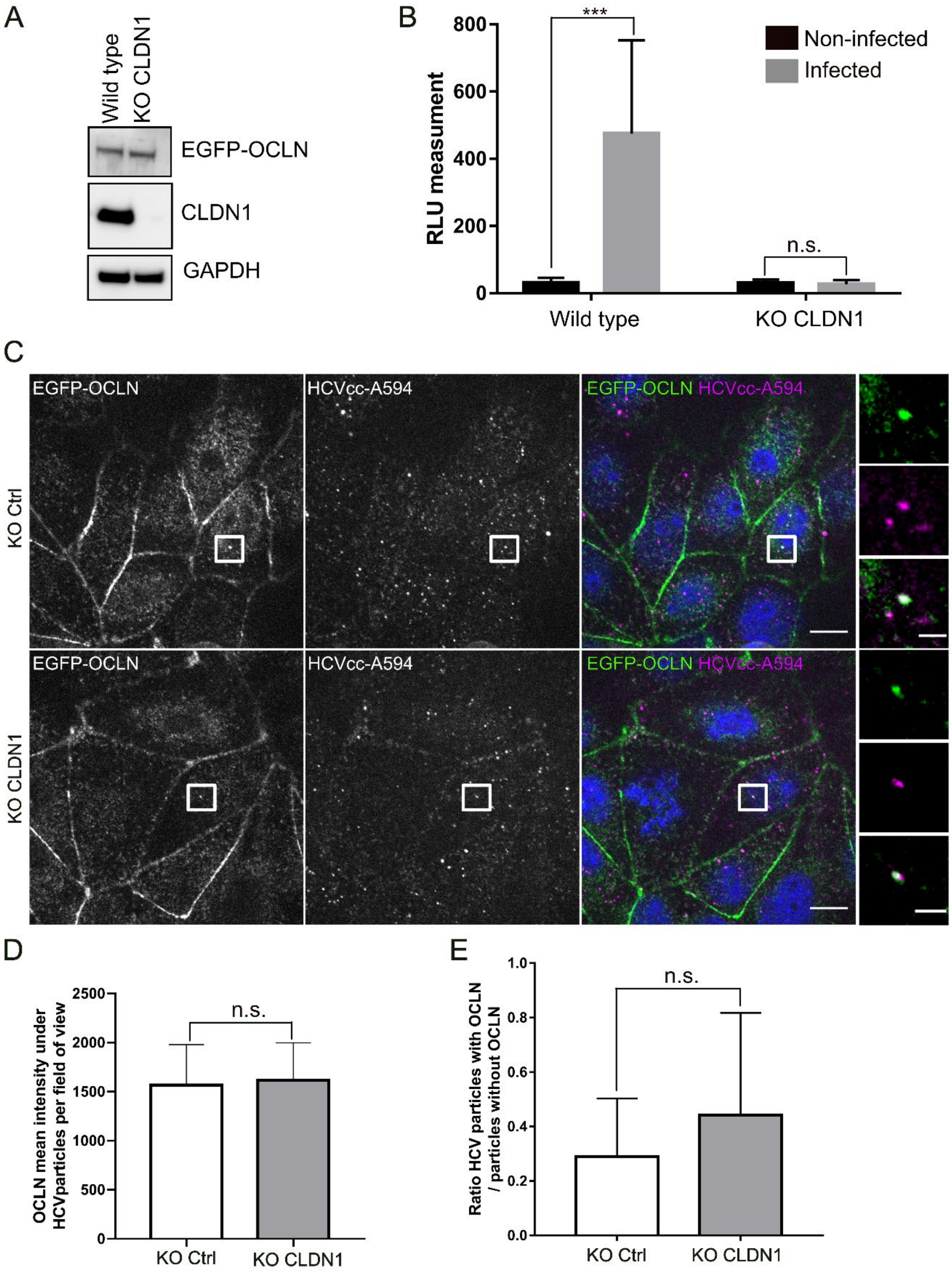
A
Wild type
KO CLDN1
EGFP-OCLN
CLDN1
GAPDH
B
***
800
600
400
200
0
RLU measument
Non-infected
Infected
n.s.
Wild type
KO CLDN1
C
EGFP-OCLN
HCVcc-A594
EGFP-OCLN HCVcc-A594
KO Ctrl
KO CLDN1
D
2500
2000
1500
1000
500
0
OCLN mean intensity under HCVparticles per field of view
n.s.
KO Ctrl
KO CLDN1
E
1.0
0.8
0.6
0.4
0.2
0.0
Ratio HCV particles with OCLN / particles without OCLN
n.s.
KO Ctrl
KO CLDN1

Figure 5

Figure 5. HCV-OCLN association in CLDN1 KO cells. (A) Lysates from Huh7.5.1 EGFP-OCLN$^{\text{edit}}$ wild type cells and Huh7.5.1 EGFP-OCLN$^{\text{edit}}$ KO CLDN1 edited cells were collected and processed for western blotting. Mouse Anti-EGFP was used to visualize EGFP-OCLN, Rabbit anti-CLDN1 was used to verify CLDN1 knock-out, and mouse anti-GAPDH was used as a loading control. (B) Huh7.5.1 EGFP-OCLN$^{\text{edit}}$ wild type cells and Huh7.5.1 EGFP-OCLN$^{\text{edit}}$ KO CLDN1 cells were infected with HCVcc-Jc1 Luc for 3 days. Luciferase activity was measured and represented as relative luciferase activity in the bar graph. Black bars represent the non-infected conditions while grey bars represent the infected conditions. Student t-test statistics were used. (***) p value < 0.001, and n.s = non-significant. (C) Huh7.5.1 EGFP-OCLN$^{\text{edit}}$ wild type cells and Huh7.5.1 EGFP-OCLN$^{\text{edit}}$ KO CLDN1 edited cells were imaged using spinning disk confocal microscope. Representative images from single z-stacks indicated EGFP-OCLN (grey or green in merge panel), HCVcc-A594 (grey or magenta in merge panel), DAPI staining for nuclei (blue in merge panel). White squares indicated the colocalization between EGFP-OCLN and HCVcc-A594. Zoom in regions from the white square are represented in left panels. Scale bars = 10 µm in the merged panel and scale bars = 2 □m in left zoomed panels. (D) Bar graph representing total OCLN mean intensity measured under HCVcc_A594 particles in Huh7.5.1 EGFP-OCLN$^{\text{edit}}$ wild type cells (EGFP-OCLN) and Huh7.5.1 EGFP-OCLN$^{\text{edit}}$ KO CLDN1. Quantification was established from experiment in (C). 22 field of views from n = 2 independent experiments were used for measurements. Error bars corresponded to SD values. n.s = non-significant was obtained from statistical Student t-test. (E) Bar graph representing the proportion of HCVcc-A594 particles associated with OCLN versus HCVcc-A594 particles without. Quantification was established from experiment in (C) and (D). Error bars corresponded to SD values. n.s = non-significant was obtained from statistical Student t-test.

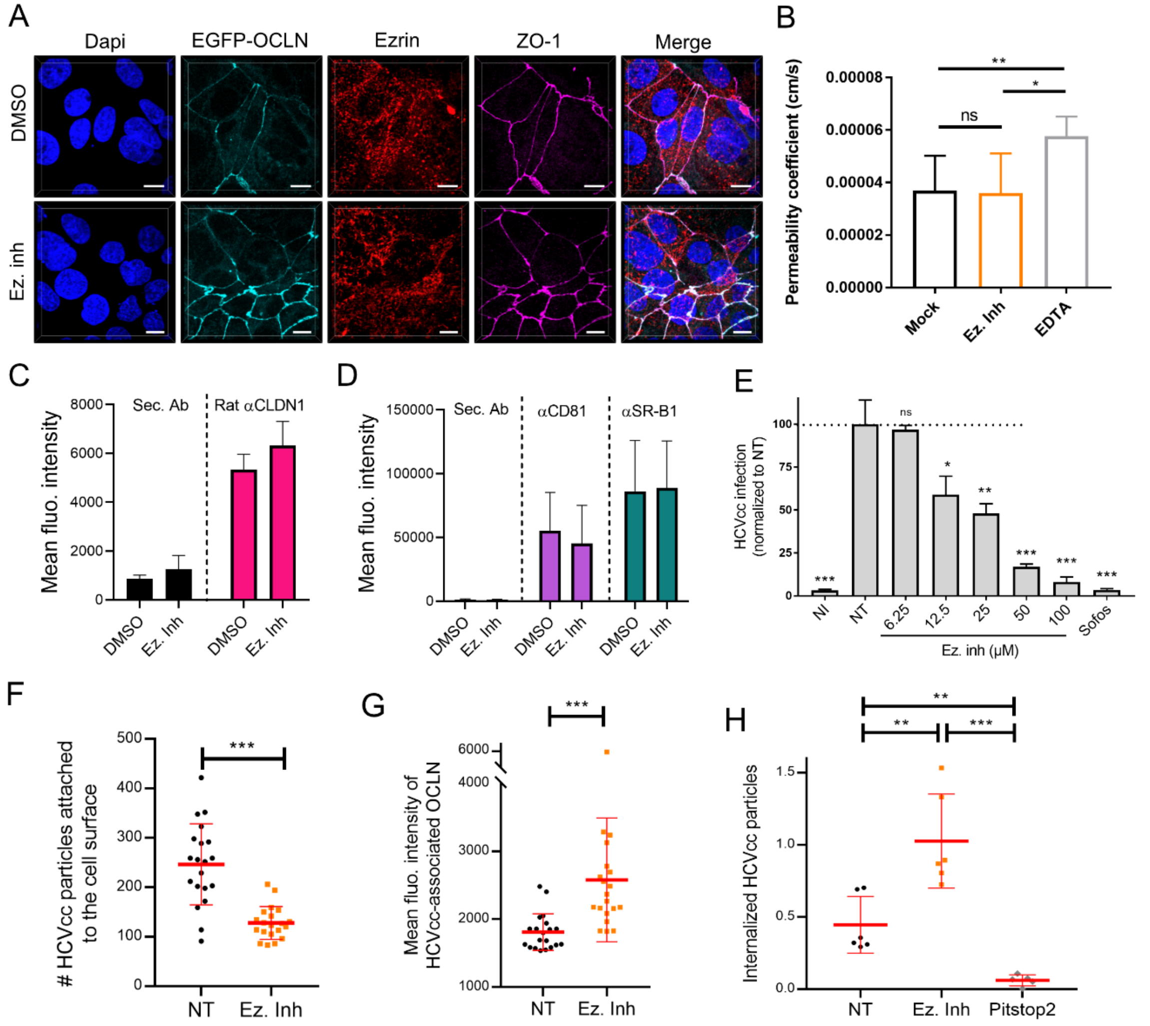

Figure 6

Figure 6. Ezrin phosphorylation is required for OCLN-HCV association and internalization outside TJs. (**A**) EGFP-OCLN^{edit} (cyan) cells were treated for 3 h with Ezrin inhibitor (Ez. Inh; lower panels) or DMSO (upper panels), fixed, permeabilized and stained using antibodies against ZO1 (magenta) and Ezrin (red), and Dapi (Blue). Three-dimensional spinning disk confocal microscopy was performed. The images represent the top view of a 3D reconstruction. Scale bar = 10 µm. (**B**) Huh7.5.1 EGFP-OCLN^{edit} cells were seeded on transwell inserts with 0.4 µm pores for 4 days. The cells were then treated for 3 h with Ez. Inh or EDTA and the permeability coefficient was assessed by measuring the Lucifer Yellow fluorescence intensity in the lower chamber (see Methods for details). The bar graph corresponds to the mean +/- SD from three experiments performed in duplicates. Two-tailed p value was non-significant (ns) or < 0.05 (*) or < 0.01 (**). (**C-D**) EGFP-OCLN^{edit} cells were treated for 3 h with 50 µM Ezrin inhibitor (Ez. Inh) or DMSO then washed and stained using primary antibodies against cell surface receptors followed by appropriate secondary antibodies. The bar graphs show mean fluorescence intensity of antibody-labelled CLDN1 (**C**; magenta), CD81 (**D**; purple) or SR-B1 (**D**; blue) on the

surface of cells treated with Ez. Inh or DMSO compared to secondary antibody staining alone (black). Data are mean +/- SD of duplicates from two or three individual experiments. No significant differences were observed between Ez. Inh and DMSO treatments. (**E**) Huh7.5.1 EGFP-OCLN^{edit} cells were treated with indicated concentrations of Ez. Inh or 5 μM Sofos, 30 min prior infection. Cells were then co-incubated with the drugs and HCVcc (Jc1-Luc) for 3 h. Cells were washed and luminescence was measured 3 days post-infection. The bar graph shows the relative HCV infection rate normalized to non-treated cells (NT). Two-tailed p value was non-significant (ns) or < 0.05 (*), < 0.01 (**) or < 0.001 (***). (**F-H**) Huh7.5.1 EGFP-OCLN^{edit} cells were treated for 3 h with 50 μM Ez. Inh or DMSO (NT). Each dot corresponds to a field of view. The red bar shows the mean +/- SEM from 20-22 fields of view per condition. The graphs show the total number of HCVcc detected at the cell surface (**F**) and the EGFP-OCLN mean fluorescence intensity of HCVcc-associated OCLN (**G**). (**H**) Huh7.5.1 EGFP-OCLN^{edit} cells were treated for 30 min with 50 μM Ez. Inh or 50 μM Pistop2 or DMSO (NT) prior infection. Cells were then co-incubated with the inhibitors and HCVcc (Jc1$^{FLAG-E2}$) for 4 h. Cell surface was cleared of non-internalized viruses using Trypsin and RT-qPCR was performed to detect relative quantity of HCV RNA. The bar graph shows the relative HCV infection rate normalized to non-treated cells (NT). Two-tailed p value was non-significant (ns) or < 0.05 (*), < 0.01 (**) or < 0.001 (***).